Electronic structure and bonding in hexagonal boron nitride



2006 J. Phys.: Condens. Matter 18 97

(http://iopscience.iop.org/0953-8984/18/1/007)

INSTITUTE OF PHYSICS PUBLISHING JOURNAL OF PHYSICS: CONDENSED MATTER

J. Phys.: Condens. Matter **18** (2006) 97–115 doi:10.1088/0953-8984/18/1/007

# Electronic structure and bonding in hexagonal boron nitride

**N Ooi[1], A Rairkar[2], L Lindsley[2] and J B Adams[2]**

[1] Department of Chemical and Materials Engineering, Ira A Fulton School of Engineering and Applied Sciences, Arizona State University, BOX 876006, Tempe, AZ 85287-6006, USA
[2] Science and Engineering of Materials Program, Center for Solid State Science, Arizona State University, BOX 871704, Tempe, AZ 85287-1704, USA

E-mail: Newton.ooi@asu.edu

Received 13 September 2005
Published 9 December 2005
Online at stacks.iop.org/JPhysCM/18/97

**Abstract**

The bonding, cohesive, and electronic properties of hexagonal boron nitride were studied using density functional theory calculations. The properties of this system were calculated using three different exchange–correlation functionals (local density approximation and two forms of the generalized gradient approximation) to determine their relative predictive abilities for this system. In-plane and interplanar bonding was examined using band diagrams, the density of states, and the electron localization function. Different stackings, or arrangements of one basal plane with respect to another, were examined to determine how the bonding and electronic structure changed between different stackings. Calculated band gaps were in the 2.9–4.5 eV range and predominantly indirect, regardless of stacking or the exchange–correlation functional used. The calculated band gaps are in the low range of experimental band gap values, and do not explain the large range of experimental values.

(Some figures in this article are in colour only in the electronic version)

## 1. Introduction

Hexagonal BN [1] (h-BN or $\alpha$-BN) has similar bonding and structure to graphite and is sometimes referred to as white graphite. Hexagonal rings form basal planes, with every B atom bonded to three N atoms in the plane and vice versa. The strong directional bonding between adjacent coplanar atoms shows charge localization closer to the N atom than the B atom, and depending on the radii assumed for each atom, each B atom loses 1–2 electrons to its three neighbouring N atoms. Electrons in $\pi$ orbitals are also localized closer to the N atoms than the B atoms [2]. Interplanar bonding is very weak with no directional bonds [3] present, and is probably a mixture of ionic attraction between oppositely charged ions in adjacent planes, and van der Waals bonding such as in graphite. The lattice constants are

  

$a_0 = b_0 = 2.50$–$2.51$ Å, and $c_0 = 6.66$–$6.67$ Å, which is very similar to those of graphite: $a_0 = 2.5$ Å and $c_0 = 6.7$ Å. The range of values reflects the difficulty in obtaining pure h-BN in polycrystalline form without the presence of amorphous BN or the other crystalline phases.

Hexagonal BN [4] has a melting point of >3000 K, and is an electrical insulator and an excellent thermal conductor. It can be produced by several methods: chemical reactions between boron compounds and nitrogen compounds [5] (e.g. boric acid + urea), hot pressing, combustion synthesis [6], and chemical vapour deposition [7]. The ease of sliding between basal planes makes it a great solid lubricant [8] for reducing wear and friction, and it can be added to other solid/liquid lubricants for machining processes [9]. There is literature [10] showing that it is more stable than graphite in high pressure–temperature machining. Its high melting temperature and low coefficient of thermal expansion make it useful in vacuum technology, and as crucible coatings [11] for holding molten metals. Hexagonal BN is also the basis for BN nanotubes [12] which is a growing area of research.

There are several unknown properties of h-BN. First, the band structure is uncertain, with even the band gap energy in doubt. Experimental reports of the band gap range from 3.0 to 7.5 eV with recent publications giving values of 3.6 [13], 4.02 [14], 5.97 [15], and 6.0 eV [16], with some publications reporting a direct band gap [15] and others reporting an indirect gap [14]. Related to this, the electron affinity is also unknown. Second, the optimal stacking(s) in h-BN is (are) unknown. Each basal plane in h-BN consists of both B and N atoms and there are many ways in which one plane can be placed above the adjacent plane. Different arrangements represent different stackings, some of which have been observed experimentally, and/or theoretically studied. One layer can slide/rotate with respect to the other plane to give different stackings. Unlike graphite, where the only stable stacking is where half the atoms in one plane lie above half the atoms in the adjacent plane, the stable stacking(s) of h-BN are not known. Several publications have proposed specific stackings, but there is no clear agreement in the literature.

Last, density functional theory (DFT) studies of h-BN have predominantly used the local density approximation (LDA) assuming as for graphite that the generalized gradient approximation (GGA) does not reliably describe interplanar bonding. This practice is premised on the belief that h-BN basal planes are held together by van der Waals bonding, just as in graphite. Yet, there is no thorough examination of why the LDA should be used for h-BN instead of the GGA, or if even interplanar bonding in h-BN is primarily van der Waals in nature. We have therefore performed a series of calculations to address these deficiencies, and in an effort to further understand the properties of h-BN. We compared several different stackings to determine which are most likely to exist, and whether they differ greatly in cohesive energy ($E_C$). We also examined the density of states (DOS), and band diagram for different stackings using the LDA and two different GGA functionals to determine how each reproduces in-plane and interplanar bonding in h-BN.

Nine different stacking were examined as part of this work; see figure 1. All views are of the primitive unit cell, which consists of four atoms divided among two parallel planes, one B and one N per plane. The AC stacking differs from the rest in that it does not produce the hexagonal rings upon use of periodic boundary conditions. This was included for illustrating the different atoms in a given unit cell; no calculations were performed on this structure. The point and space group symmetries for each stacking are provided in table 1 for both the Hermann–Mauguin notation and Schoenflies notation.

The different stackings can be classified in two different ways; see table 2. The first way is to group the stackings according to how atoms in one plane sit atop atoms of the adjacent plane. This gives three classes: A1, A2, and A3, where A stands for atop, as in how atoms in one plane are situated atop atoms in the adjacent plane. The first class (A1) is where each atom

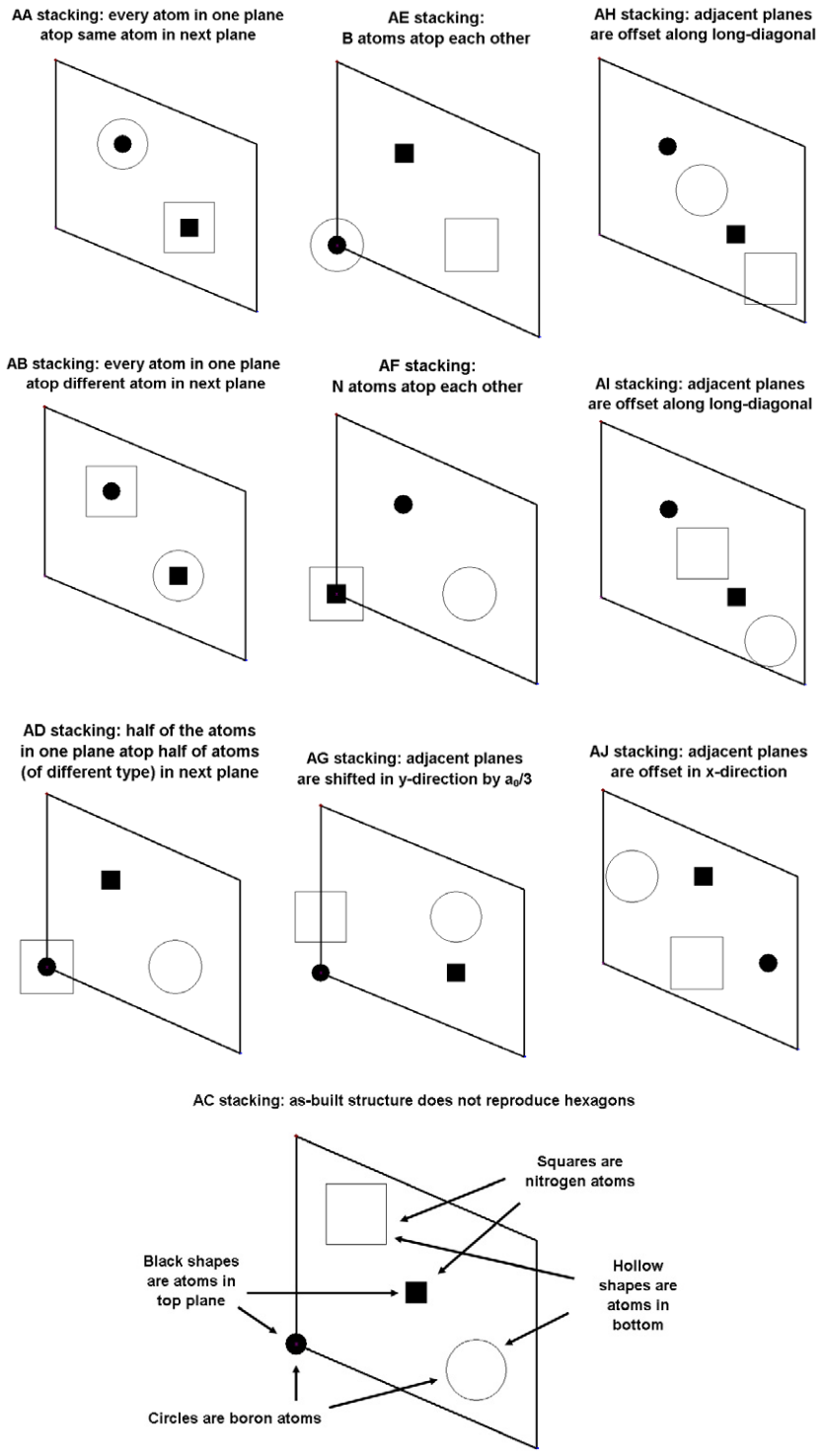


**Figure 1.** Different stackings (structures) of h-BN viewed in the (0001) direction.

**Table 1.** Symmetries of different h-BN stackings.

| | Hermann–Mauguin | | Schoenflies | | | |
|---|---|---|---|---|---|---|
| Stacking | Space group | Point group | Point symmetry | Point group | A group | T group |
| AA | $P\bar{6}m2$ | $\bar{6}m2$ | $D_{3h}$ | X | A1 | T1 |
| AB | $P63/m2/m2/c$ | $6/mmm$ | $D_{3d}$ | $D_{6h}$ | A1 | T2 |
| AC | $P1$ | 1 | $C_{1h}$ | $D_{2h}$ | X | X |
| AD | $P3m1$ | $3m1$ | $C_{3v}$ | $D_{3h}$ | A2 | T1 |
| AE | $P63/m2/m2/c$ | $6/mmm$ | $D_{3d}$ | $D_{6h}$ | A2 | T2 |
| AF | $P63/m2/m2/c$ | $6/mmm$ | $D_{3d}$ | $D_{6h}$ | A2 | T2 |
| AG | $P121/m1$ | $2/m$ | $C_{1}$ | $C_{2h}$ | A3 | T2 |
| AH | $C2/m2/c21/m$ | $Mmm$ | $C_{1h}$ | $C_{2v}$ | A3 | T1 |
| AI | $C2/m2/c21/m$ | $mmm$ | $C_{1h}$ | $D_{2h}$ | A3 | T2 |
| AJ | $P121/m1$ | $2/m$ | $C_{2h}$ | $D_{2h}$ | A3 | T2 |

**Table 2.** Simulation details and results of recent DFT studies of h-BN (X = not listed).

| | | | | Band gap | | | | |
|---|---|---|---|---|---|---|---|---|
| Reference | XC | PP | h-BN stacking | eV | Type | $a_0$ (Å) | $c_0$ (Å) | $E_C$ (eV) |
| Mosuang *et al* | LDA | NC | AA | X | X | 2.499 | 7.582 | X |
| | | | AB | X | X | 2.503 | 6.838 | X |
| | | | AF | X | X | 2.499 | 7.092 | X |
| Furthmuller *et al* | LDA | NC | AB | X | X | 2.481 | 6.470 | 8.133 |
| | | US | AB | 4.1 | H–M | 2.486 | 6.439 | 8.097 |
| Xu *et al* | LDA | X | Unknown | 4.07 | H–M | 2.494 | 6.66 | X |
| Kim *et al* | Both | NC | Unknown | X | X | 2.513 | 6.433 | 8.256 |
| Janotti *et al* | LDA | X | AB | X | X | 2.495 | 6.437 | 8.081 |
| | GGA | X | AB | X | X | 2.517 | 8.397 | 7.006 |
| Liu *et al* | LDA | US | AA | 3.226 | K–L | 2.485 | 6.912 | X |
| | | | AB | 4.027 | H–M | 2.485 | 6.49 | X |
| | | | AD | 4.208 | H–M | 2.485 | 6.423 | X |
| | | | AE | 3.395 | K–K | 2.484 | 6.487 | X |
| | | | AF | 3.433 | K–M | 2.484 | 7.048 | X |
| Cappellini *et al* | LDA | NC | X | X | X | 2.486 | 6.484 | X |
| Ohba *et al* | LDA | US | AB | X | X | 2.496 | 6.498 | 7.943 |
| Yu *et al* | LDA | US | AB | X | X | 2.481 | 6.491 | 7.973 |
| Kern *et al* | LDA | US | AB | X | X | 2.489 | 6.481 | 8.093 |

in one layer lies directly above an atom in the adjacent layer. The second class (A2) is where half the atoms in one layer lie directly above half the atoms in the adjacent layer. The third class (A3) is where none of the atoms in a layer lie directly above any atoms in the adjacent layer. The stackings can also be grouped into two groups labelled T1 and T2 where T stands for translation, as each member of that group can be translated to any other member of that group without a rotation. Stackings in the T1 group are interchangeable by translation parallel to a cell edge. Stackings in the T2 group are also interchangeable by translation parallel to a cell edge. But a stacking in the T1 group must be rotated by 60° in order to be translated into a stacking in the T2 group, and vice versa.

## 2. Review of theoretical work

The increasing use of the various phases of BN has inspired many theoretical studies of their properties. Many of these studies used the Hohenberg–Kohn–Sham formulation of DFT [17] with the exchange–correlation (XC) energy calculated by the LDA or some form of the GGA. We review some recent DFT studies of h-BN and table 2 provides a comparison of their simulation details and calculated properties. The stackings used in these publications are referred to here according to figure 1.

Furthmuller *et al* [18] used plane waves (PW) with ultrasoft (US) and norm-conserving (NC) pseudopotentials (PP) to calculate the structural, cohesive, and electronic properties of the different BN phases. Kern *et al* [19] followed this up by calculating the lattice dynamics and phase diagram of BN. They derived the ($P$, $T$) phase diagram of BN in the quasiharmonic approximation using electronic and vibrational energies at different volumes. Kim *et al* [20] studied the stability of cubic, hexagonal, and wurtzite BN using PW-PP calculations and found that c-BN is the stable phase at 0 K. Cappellini *et al* [21] calculated optical properties such as dielectric functions of BN in the cubic and hexagonal phases using PW-PP calculations. The previously listed publications all predict that c-BN is more stable than h-BN at 0 K and this trend is supported by other publications [22–26].

Some have proposed that the discrepancies in the h-BN electronic structure are due to different stackings. Liu *et al* [27] investigated the relative stabilities of five different h-BN stackings at 0 K using PW-PP calculations. The calculated equilibrium lattice constants of all five were very similar though they had slightly different band structures. Discrepancies in experimentally measured band structures are ascribed to the fact that actual h-BN, even if crystalline, is probably a mixture of the different stackings, each with a unique band diagram.

There have only been a few studies of h-BN using a local orbital basis set, and only one that examined the band structure. Xu *et al* [28] compared the properties of h-BN, c-BN, and w-BN using an orthogonalized LCAO basis. Orbitals were included up to the 3s and 3p for both N and B atoms. The band structures, density of states, charge density, and dielectric function for all three allotropes were examined and compared to each other and to available experimental data. They determined that all three allotropes have an indirect band gap. These previous DFT studies on h-BN have predominantly examined the AB stacking, even though many stackings are possible. Also, previous DFT-calculated band gap values for h-BN are at the low end of the experimental range, and do not explain the large range of theoretical values. Because of these two drawbacks, we have examined nine stackings of h-BN using both the LDA and GGA to determine if the large range of measured band gaps can be accounted for by different stackings, or can be reproduced by using the GGA instead of the LDA.

## 3. Methodology

We used the Vienna Ab initio Software Package (VASP) [29] to perform our calculations. The wavefunctions were expanded in a plane wave basis set and used with projected augmented wave (PAW) [30, 31] pseudopotentials [32]. The exchange–correlation energy was approximated using either the LDA adapted by Ceperley and Alder [33], the GGA of Perdew and Wang (PW91) [34] or the GGA of Perdew, Burke, and Ernzerhof (PBE) [35]. Energies of the irreducible Brillouin zone (BZ) were sampled with a Gamma-centred $k$-mesh. Ground state energies and charge densities were calculated self-consistently using a Pulay-like mixing scheme [36] and the blocked Davidson minimization algorithm [37, 38]. Initial charge densities were taken as a superposition of atomic charge densities. Hexagonal BN is an insulator, so temperature smearing was not used for any calculations and the occupation of electronic states was set using the linear tetrahedron method with Blochl corrections [39].

**Table 3.** Irreducible $k$-points for the different stackings using different mesh sizes.

| Stackings | $6 \times 6 \times 6$ mesh | $8 \times 8 \times 8$ mesh | $10 \times 10 \times 10$ mesh |
|---|---|---|---|
| AH, AJ, AI | 52 | 105 | 186 |
| AA, AB, AD, AE, AF | 28 | 50 | 84 |
| AG | 80 | 170 | 312 |

**Table 4.** Comparison of h-BN stackings at $a_0 = 2.5$ Å and $c_0 = 6.66$ Å.

| | PBE | | PW91 | | LDA | |
|---|---|---|---|---|---|---|
| Stacking | $E_C$ (eV/atom) | $P$ (kB) | $E_C$ (eV/atom) | $P$ (kB) | $E_C$ (eV/atom) | $P$ (kB) |
| AA | 7.019 | 26 | 7.072 | 18 | 7.972 | −52 |
| AB | 7.036 | 22 | 7.089 | 13 | 7.989 | −56 |
| AD | 7.036 | 20 | 7.089 | 12 | 7.989 | −58 |
| AE | 7.034 | 20 | 7.087 | 12 | 7.988 | −58 |
| AF | 7.022 | 25 | 7.075 | 17 | 7.975 | −53 |
| AG | 7.031 | 22 | 7.084 | 14 | 7.984 | −56 |
| AH | 7.029 | 23 | 7.082 | 14 | 7.982 | −55 |
| AI | 7.029 | 23 | 7.082 | 15 | 7.983 | −55 |
| AJ | 7.033 | 21 | 7.086 | 13 | 7.987 | −57 |

## 4. Comparison of different simulation settings

Two calculations were performed on each stacking, one with, and one without spin polarization, to determine whether spin polarization is required. For each stacking, final enthalpies differed by less than 0.1 meV/atom and the cell magnetic moment was zero. This is expected as there are no unpaired valence electrons in h-BN. Spin polarization was not included in further calculations to reduce computational cost. Plane wave convergence to 1 meV/atom was reached at or below 420 eV for all stackings so for consistency, all future calculations used a 420 eV cut-off. k-point convergence to 1 meV/atom was reached with a $10 \times 10 \times 10$ mesh or smaller for all stackings and table 3 gives the number of irreducible points for each mesh.

## 5. Comparison of different stackings

Calculations were performed to determine the relative stabilities of different stackings. The total energies and cell pressures ($P$) were obtained on each stacking using the most commonly cited values for the experimental lattice constants: $a_0 = 2.5$ Å and $c_0 = 6.66$ Å, to see whether any of them can be ruled out as being unstable. The $E_C$ (eV/atom) was obtained by subtracting the spin-polarized enthalpies of the free B and N atoms from the total energy of the cell. Table 4 provides the calculated $E_C$ and $P$ (kilobars—kB) values. The different pressures obtained for each stacking suggest each has a different set of equilibrium lattice constants depending on the XC functional used. LDA-calculated pressures are negative for all stackings, indicating that the cells are in tension and the equilibrium volumes are less than the experimental values. Both GGA functionals give positive pressures, indicating that the cells are in compression, and would lower their energies by expanding their volumes from its experimental value. The LDA overbinds and this overbinding were compensated for by using the GGA, which actually predicts underbinding in this case as the cell pressures are all in compression.

For all stackings using any functional, forces on atoms perpendicular to the basal plane were zero. In-plane forces were exactly zero for AA, AB, AD, AE, and AF, but were non-zero

for AG, AH, AI, and AJ. Therefore, AG, AH, AI, and AJ can be considered as unstable and might be transition states in basal plane sliding. All the unstable stackings have atoms in one plane above the bonds of the adjacent plane, whereas all the stable stackings have atoms in one plane above atoms or the ring hole of the adjacent plane. The electron density in the bonds seems to repel the atoms in adjacent planes, and this could be due to electron delocalization. Specifically, the valence electrons try to maximize their separation by increasing their volume of occupation. This lowers their kinetic energy and hence the total energy. Delocalization is best accomplished if the bonds are not above atoms in the adjacent plane. By electrostatic arguments, AB and AD would be stable stackings because oppositely charged ions in adjacent planes are atop each other. AA is most likely metastable because identical ions are atop each other, and AE and AF could be either stable or metastable. These suppositions were checked by running simulations on each of these five stackings in which one plane was displaced about 0.001 Å in the $x$-direction from its as-built position, and calculating the total energy and forces on the atoms. Results from the calculations showed that AB and AD are stable in that the displaced plane moves back to its original position. AA, AE, and AF are metastable in that the displaced plane stays displaced.

## 6. Bonding and electronic structure

The anisotropic bonding in h-BN allows the bonding in different directions to be analysed separately. Specifically, the DOS and band diagram can be obtained on a single plane of h-BN. This is achieved using a two-atom hexagonal unit cell with $a_0 = 2.5$ Å and $c_0 = 10$ Å to minimize interaction between the plane and its periodic images in the neighbouring cells. In this way, the resulting DOS and band diagram are due to in-plane bonding only. The electronic structure can then be obtained on the four-atom unit cell containing two planes per cell. This introduces interplanar bonding, and the difference in the electronic structure between the isolated plane and the four-atom unit cell is due to interplanar bonding. The DOS, projected DOS (PDOS) on both the B and N atoms, and the band diagram were obtained on the isolated plane and the four-atom unit cell using each of the three XC functionals, and were compared to see how the three functionals modelled in-plane and interplanar bonding.

The wavefunctions and charge density for each stacking were generated first without any Fermi level smearing. These were used as input into a second calculation to determine the eigenvalues along the high symmetry directions. The resulting eigenvalues were used for plotting the $k$-space band diagrams. These calculations along specific regions of the BZ precluded the use of space-filling tetrahedra; so they used 0.01 eV Gaussian smearing. Therefore, the band gaps from the $k$-space diagrams include Fermi level smearing, and are not as accurate as that obtained from the DOS. The $k$-space band diagrams do provide the type of band gap which cannot be obtained from the DOS. Calculated eigenvalues were identical using either 0.01 eV Methfessel–Paxton [40] or Gaussian smearing, suggesting that the smearing method does not affect the results. Each stacking had a different pressure in the $E_C$ calculations; therefore each stacking has its own equilibrium lattice constants. The issue then arises as to which lattice constants to use for plotting the band diagrams. For consistency and simplicity, the electronic structure are obtained on the four-atom unit cell for each stacking at $a_0 = 2.5$ Å and $c_0 = 6.66$ Å.

### *6.1. DOS of isolated plane*

The DOS of the isolated plane using the three functionals are plotted together in figure 2. They are very similar in that they show the same features, band widths, and band gaps. All show the core levels in the $-21$ to $-17$ eV range, the valence band (VB) in the $-12$ to $-3$ eV range, and

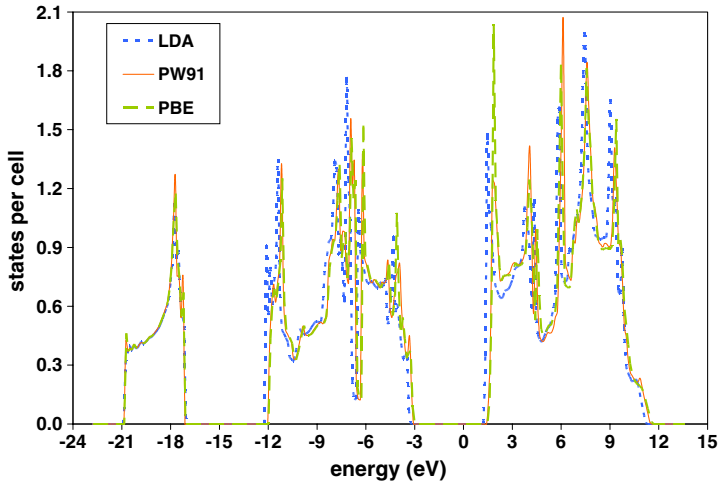


**Figure 2.** DOS of a single plane of h-BN using three different XC functionals.

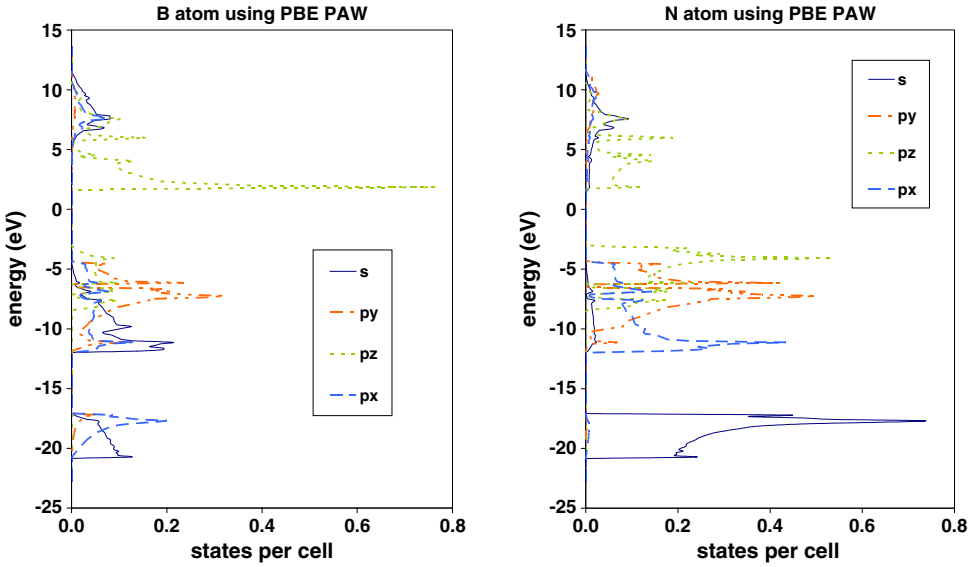


**Figure 3.** PDOS on different atoms in a single plane of h-BN.

the conduction band (CB) in the 1–12 eV range. The heights of the different peaks in each of the three bands are also very similar for different functionals. The most noticeable differences occur at the CB minimum where a high peak exists for the PBE, but is shorter for the LDA and PW91, but even these differences are minor.

The PDOS on B and N atoms are shown in figure 3. Several features are common to all the functionals. First, there is clear $sp^2$ hybridization in the VB and CB on both atoms due to the s and p peaks having overlapping energy ranges. Second, the CB–VB band gap on either B or N is defined by the $p_Z$ peaks in both bands, suggesting that the most likely electronic excitation in h-BN is from the $2p_Z$ orbital to the $3p_Z$ orbital. Third, on N atoms, p peaks are highest in the VB and weakest in the core levels. This makes sense as the N core state is

**Table 5.** Relative sizes of peaks of each $m_l$ component in the PDOS.

| Boron atom | | Nitrogen atom | |
|---|---|---|---|
| $m_l$ component | Relative heights | $m_l$ component | Relative heights |
| s | VB > core > CB | s | Core > CB > VB |
| $p_X$ | Core > VB > CB | $p_X$ | VB > CB > core |
| $p_Y$ | VB > core > CB | $p_Y$ | VB > CB > core |
| $p_Z$ | CB > VB > core | $p_Z$ | VB > CB > core |

**Table 6.** Relative sizes of different $m_l$ components in each band in the PDOS.

| Boron atom | | Nitrogen atom | |
|---|---|---|---|
| Band | Relative heights | Band | Relative heights |
| Core | $s > p_X > p_Y > p_Z$ | Core | $s > p_X > p_Y > p_Z$ |
| VB | $p_Y > s > p_Z > p_X$ | VB | $p_X \sim p_Y \sim p_Z > s$ |
| CB | $p_Z > s > p_X > p_Y$ | CB | $p_Z > s > p_Y \sim p_X$ |

comprised of 1s electrons with minimal p character. In the VB, N has five valence electrons in a $2s^2p^3$ configuration, and the extra charge it withdraws from adjacent B atoms go into the 2p orbitals, thereby raising the 2p peaks in the VB. This also explains why on N atoms, all three 2p peaks are of similar height whereas on B atoms, the $2p_Z$ is lower than the $2p_Y$ and $2p_X$. To be more exact, each atom in h-BN has $s + p_X + p_Y = sp^2$ hybridization in its $n = 2$ valence orbitals. B atoms do not have any electrons in its unhybridized $2p_Z$ orbital. With five valence electrons, an N atom has charge in its $2p_Z$ orbital when it bonds with B atoms. This will raise the $p_Z$ peaks in the VB of N atoms with respect to the $p_Z$ peak in B atoms.

The presence of p peaks in the B core level indicates that there is some mixing of the 2p states with the 1s states. This can be explained by the loss of electrons from B to N in h-BN. Specifically, each B atom loses charge from its $n = 2$ level to adjacent N atoms. The reduced electron density on B means that each valence electron sees less screening of the nucleus than in the free B atom. Reduced screening means that the nucleus pulls more strongly on the remaining electrons, so the valence orbitals move inwards. The valence orbitals include p orbitals; hence the p peaks in the core levels. B atoms have strong $p_X$ peaks in all three bands such that the peaks have similar widths and heights. This is different for N atoms, where the largest $p_X$ peaks are in the VB, followed by much smaller peaks in the CB, and almost negligible peaks in the core levels. Similarities and differences in the PDOS are summarized in tables 5 and 6. In table 5, the different bands are arranged according to the relative size of specific peaks in that band. In table 6, the different peaks within each band are arranged by their relative sizes.

There are minor differences in the PDOS between different functionals. The most noticeable difference is that the highest peak in the B PDOS is approximately the same height as the highest peak in the N PDOS using the PBE. This is not true using the LDA or PW91, where the highest peak in the N PDOS, the 1s peak, is higher than the highest peak in the B PDOS, the $3p_Z$. We are unsure of the reason(s) for this. The only other differences in the PDOS between the three XC functionals were slight changes in relative peak heights and positions. These similarities in the PDOS indicate that in-plane bonding is modelled very similarly by all three XC functionals, so only the PBE data are plotted.

### *6.2. Band diagrams of isolated h-BN plane*

Like the PDOS data, the band diagrams of the h-BN plane as obtained for each functional are nearly identical to each other. All show similar dispersion, band curvature, band widths, and

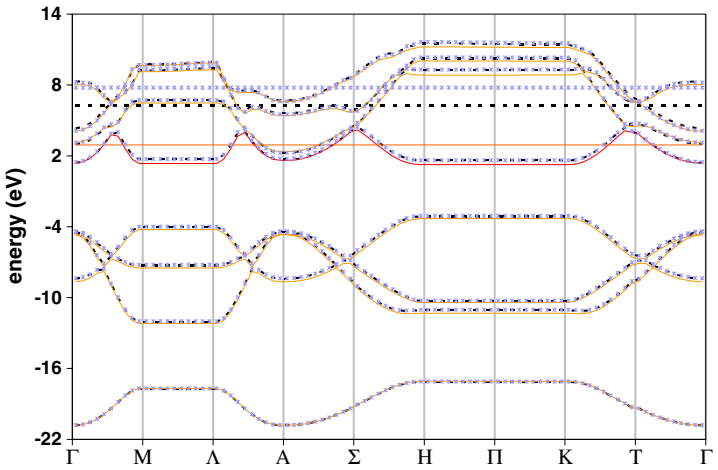


**Figure 4.** Band energies of single h-BN plane calculated using the different XC functionals and superimposed onto one band diagram.

**Table 7.** Band properties (eV) of a single h-BN plane.

| | Data obtained from DOS | | | | Data obtained from band diagrams | | |
|---|---|---|---|---|---|---|---|
| XC functional | Core width | VB width | CB width | Band gap | VB max | CB min | Band gap |
| PBE | 3.64 | 8.83 | 10.20 | 4.49 | $\pi$–K | Γ | 4.54 |
| PW91 | 3.63 | 8.84 | 10.17 | 4.48 | $\pi$–K | Γ | 4.53 |
| LDA | 3.72 | 8.89 | 9.97 | 4.57 | K | H–K | 4.58 |

band gaps at each high symmetry $k$-point. The LDA bands are solid orange lines, the PW91 bands are black broken lines, and the PBE bands are blue X symbols in figure 4. The vacuum level for each functional is the flat horizontal line of the same type and colour. The band gaps and widths as calculated from the DOS and band diagrams are given in table 7. The CB–VB gap is indirect for each functional and ∼4.5 eV. The band gap is nearly identical between the PW91 and PBE, with the PBE gap about 0.1 eV higher. The LDA band gap is ∼0.5 eV higher than the GGA gaps from the band diagrams.

One difference in the band diagrams is as regards the location of the VB maximum and CB minimum. The LDA has the VB maximum at K, and the CB minimum in the H–K region. For the GGA, the CB minimum is at Γ while the VB maximum is in the $\pi$–K region. This difference, though present, is very small. Specifically, the CB minimum at Γ is within 0.01 eV of the CB minimum in the H–K region for all three functionals. Likewise, the VB maximum is very similar throughout the $\pi$–K region for all three functionals. Another difference in the bands predicted by the three functionals is as regards the vacuum level. The vacuum is entirely within the CB for PW91 only. In the LDA, the vacuum is below the CB at certain points in the BZ, and inside the CB at other points in the BZ. The opposite occurs for the PBE diagram; here the vacuum is above the CB in certain regions of the BZ and inside the CB in other regions of the BZ. But in both the LDA and PBE diagrams, the vacuum level is never above/below the CB in the entire BZ. We are unsure of the reason for the differences in the vacuum level using different XC functionals. Calculations were performed to determine whether these differences

are attributable to the precision or accuracy of our simulations. First, the vacuum levels were recalculated for each stacking using a larger $15 \times 15 \times 15$ $k$-mesh for BZ sampling. Second, the vacuum levels were recalculated using a lower cut-off energy of 400 eV. These recalculated vacuum levels were within $\pm 0.1$ eV of the original values obtained with a $10 \times 10 \times 10$ $k$-mesh and a 420 eV cut-off energy, so the differences in vacuum levels between the three XC functionals are not attributable to the precision or accuracy of the calculations.

### *6.3. Electron localization in the isolated plane*

The spatial distribution of electrons into core, non-bonding, and bonding orbitals can be visualized using the electron localization function (ELF). Becke and Edgecombe [41] introduced the ELF as a measure of the probability of finding one electron near another electron with the same spin. The ELF is a contour plot in real space where different contours have values ranging from 0 to 1. A region with ELF $\sim 1$ is where there is no chance of finding two electrons with the same spin. This usually occurs in places where bonding pairs (molecular orbitals) or lone pairs (atomic orbitals) reside. An area where ELF $\sim 0$ is typical for vacuum (no electron density) or areas between atomic orbitals. This is where electrons of like spin approach each other the closest. ELF $= 0.5$ for a homogeneous electron gas and 1.0 at areas where covalent bonds or lone pairs (filled core levels) occur. The ELF is not a measure of electron density, but is a measure of the Pauli principle, and is useful in distinguishing metallic, covalent, and ionic bonding [42, 43].

The ELF was examined for the basal plane; see figure 5. Looking in the $[1\bar{1}00]$ direction, high electron localization is seen in the region between adjacent B and N atoms indicative of covalent bonding. The highest ELF values in the bond is located about halfway between the B and N atom, while the region around N has an overall higher ELF value than the region around the B atom, reflecting the ionicity in the bond with N withdrawing charge from B. The regions of ELF $\sim 1$ directly above and below the N atoms are lone pairs, and are absent on the B atoms, again reflecting the higher electron localization around N than B. One interesting phenomena is the presence of small, disconnected, circular regions of non-zero ELF above and below the basal plane. This delocalization of the electrons above and below the basal plane might be responsible for interplanar bonding in h-BN. Their distributions, shapes and sizes differ between the LDA, PBE and PAW, suggesting that the three functionals will predict interplanar bonding of different strengths.

The ELF plot on the (0001) plane provides a measure of bonding within the basal plane; see figure 6. In the plot, the hexagonal ring is delineated by a solid hexagon, with B and N atom positions indicated. The B atom and its surrounding region have a lower ELF than the N atom and its surrounding region, reflecting the ionicity in the bonding. Contours in the ring holes are not circular, but triangular in shape, with the three sides facing N atoms and the three corners pointing towards B atoms. This shape is due to electrons from the bonds and N atoms extending further into the ring hole than electrons on the B atoms. The ring hole centre is white, indicative of minimal electron density and hence localization. In contrast with interplanar bonding, the ELF plot in the basal plane is essentially identical between the LDA, PBE and PW91, suggesting that in-plane bonding is modelled the same by all three functionals, so only the LDA data are shown.

### *6.4. DOS of four-atom unit cells*

The DOS and band diagram were obtained for the four-atom unit cell to see how they differ from the isolated plane and how they change across different stackings. As in the isolated plane, the

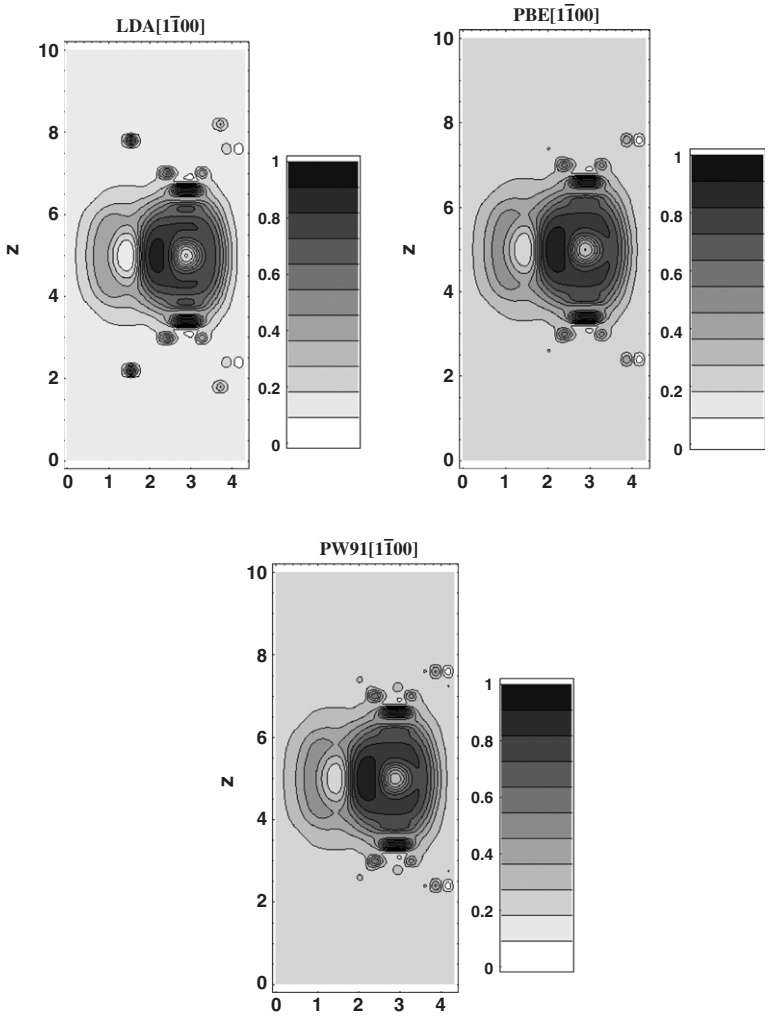


**Figure 5.** ELF on the [1$\bar{1}$00] plane.

PDOS is very similar across all three functionals, so only the PBE data are shown in figure 7. There are several similarities in the PDOS across all stackings. First, for a given functional, the PDOS on B atoms are nearly identical in the core and VB, and minor differences are noticeable in the CB only. The same is also true for the N PDOS. In DFT calculations, only the eigenvalues of occupied states (VB) factor into the total energy. Since the CB of the stackings are essentially identical, they have nearly identical total energies, hence the similarity in $E_C$ values. Together, they suggest that the change in stacking does not change the bond strength in h-BN. Second, the CB–VB gap is always between the $3p_Z$ and $2p_Z$ orbitals, indicating that the lowest energy electron transition is the same in all stackings. Last, the PDOS on the B atom has large $p_X$ and $p_Z$ peaks in the CB, whereas only the $p_Z$ peak is noticeable for the PDOS in the isolated plane.

In AA, each B (N) atom is above/below B (N) atoms in the adjacent planes so the two B (N) atoms in the unit cell are in identical environments. Therefore, the PDOS on one B (N)

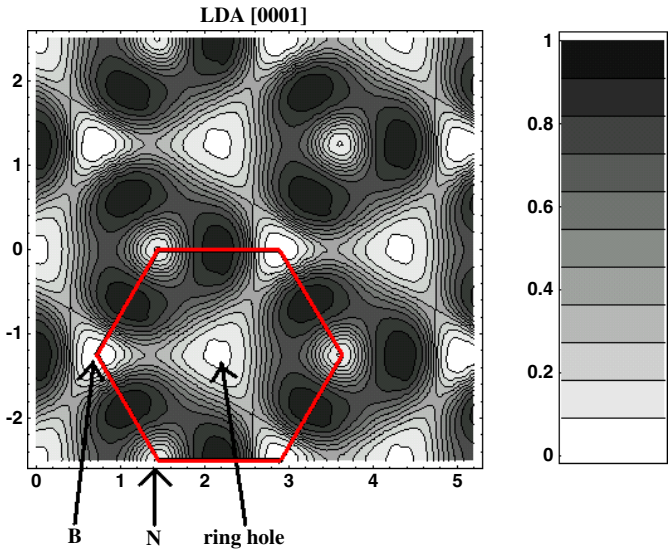


**Figure 6.** ELF on the [0001] plane.

atom is identical to the PDOS on the other B (N) atom. Similar arrangements occur in AB, AE, and AF, where the two B (N) atoms are in identical environments, and hence have identical PDOS. This is not so for the other stackings. For example, in AD half the B atoms are atop half the N atoms, but the other half of the atoms are above and below ring holes. The PDOS on the four atoms in AD are slightly different. The two B atoms are labelled B-1 and B-2, and the two N atoms are labelled N-1 and N-2. A suffix of 1 indicates that the atom is above a ring hole in the adjacent plane. A suffix of 2 indicates that the atom is above an atom in the adjacent plane. The largest difference in the PDOS between B-1 and B-2 occurs in the CB. In B-1 the $p_X$ and $p_Z$ peaks in the CB are smaller than the $p_Y$ peak in the VB, which is the largest peak in the PDOS. In B-2, the $p_X$ and $p_Z$ peaks in the CB are the largest peaks in the entire spectrum. The PDOS show more similarity between N-1 and N-2, with the only noticeable difference being the height and shape of the $p_Z$ peak in the CB.

### *6.5. Band diagrams of different h-BN stackings*

The band diagrams were examined for each stacking using each XC functional; see figure 8 and tables 8 and 9. All three XC functionals give essentially identical band diagrams for any stacking, so only the LDA and PW91 bands are plotted. The LDA bands are solid red lines and the PW91 bands are blue dotted lines. The horizontal lines are $E_F$ and the vacuum, with the vacuum above the $E_F$ in all cases. For each diagram, the $E_F$ for both the LDA and PW91 bands are set equal to each other.

Comparisons between the different diagrams showed several things. First, the PW91 and LDA bands are extremely similar to each other for each stacking, just like in the isolated plane. Second, the diagrams for all stackings and functionals were extremely similar, with all showing the VB maximum at or near K, so the band diagrams for only three stackings are shown. The main difference in the VB appeared in the H–K and M–L regions of the BZ. Specifically, some stackings, like AB, AD, and AE, had two bands touching $E_F$ in the entire H–K region. AJ had one band in contact at $E_F$ in the entire H–K region, while others like AA and AF had

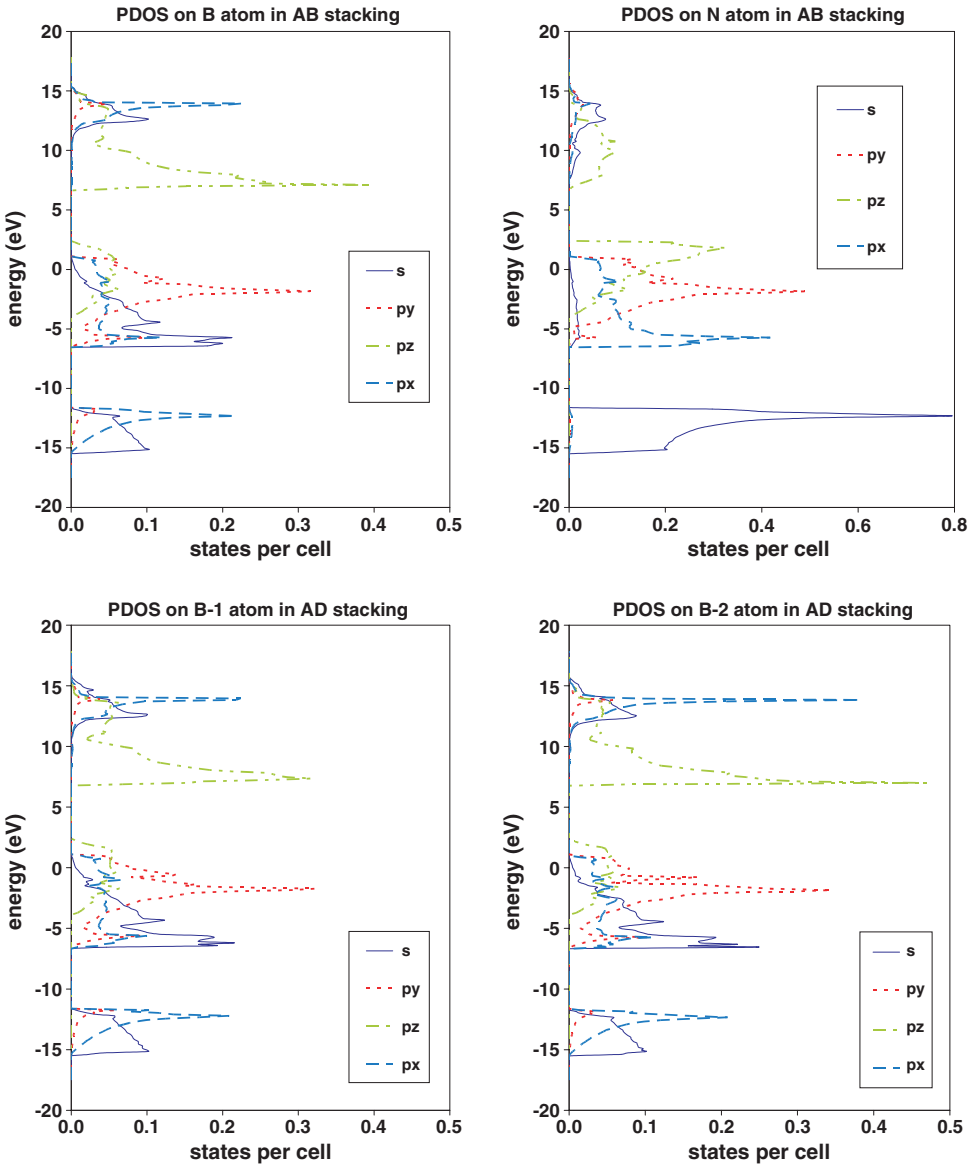


**Figure 7.** PDOS in different stackings using PBE PAW.

only one band touch $E_F$ at only the K point. Differences in the CB of different stackings were predominantly in the H–K region. The biggest difference in band diagrams between different functionals was the vacuum level was usually higher in the CB for the GGA than the LDA, such that no regions of the CB were below the vacuum. This is in contrast with LDA results where for all stackings, the vacuum is near the CB minimum such that part of the CB is above the vacuum and part is below it.

Published data on the h-BN band gap are either H–M, K–L, K–K, or K–M. The calculated band gaps for the stackings examined here include three of these, with the K–L gap not found. The two most common band gaps found in the present calculations were H–M

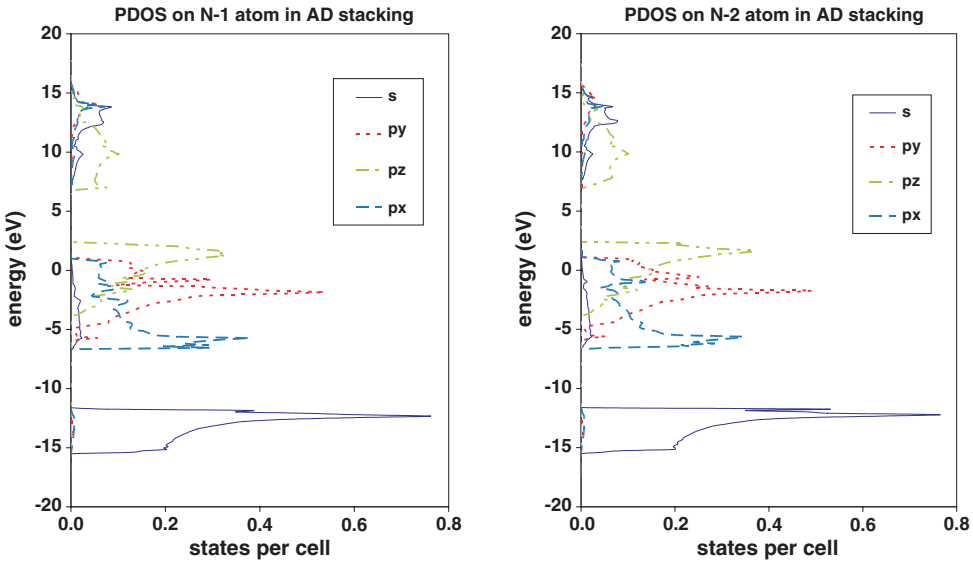


**Figure 7.** (Continued.)

**Table 8.** LDA PAW band properties (eV) from band diagrams.

| Stacking | VB max | CB min | Band gap | Vacuum |
|---|---|---|---|---|
| AA | K (2.78) | M (5.68) | Indirect (2.90) | 8.60 |
| AB | K–T (2.24) | M (6.30) | Indirect (4.06) | 8.13 |
| AD | H–P (2.26) | M (6.46) | Indirect (4.21) | 8.40 |
| AE | K–T (2.22) | K (5.70) | Indirect (3.48) | 8.39 |
| AF | K (2.78) | M (5.80) | Indirect (3.01) | 8.60 |
| AG | K–T (2.51) | M (5.71) | Indirect (3.20) | 8.45 |
| AH | K–T (2.54) | M (5.92) | Indirect (3.38) | 8.55 |
| AI | K–T (2.57) | M (5.85) | Indirect (3.28) | 8.51 |
| AJ | K–T (2.38) | K–T (6.08) | Direct (3.71) | 8.31 |

**Table 9.** GGA PAW band properties (eV) from band diagrams.

| Stacking | VB max | CB min | Band gap | Vacuum |
|---|---|---|---|---|
| AA | K (2.87) | K (5.98) | Direct (3.12) | 10.34 |
| AB | K–T (2.34) | M (6.61) | Indirect (4.28) | 10.31 |
| AD | H–P (2.35) | M (6.75) | Indirect (4.39) | 11.96 |
| AE | K–T (2.32) | K (5.97) | Indirect (3.66) | 11.91 |
| AF | K (2.87) | M (6.10) | Indirect (3.23) | 10.30 |
| AG | K–T (2.60) | M (6.01) | Indirect (3.41) | 11.92 |
| AH | K–T (2.63) | M (6.22) | Indirect (3.59) | 11.94 |
| AI | K–T (2.66) | M (6.17) | Indirect (3.51) | 10.32 |
| AJ | K–T (2.47) | K–T (6.35) | Direct (3.89) | 10.81 |

and K–M. For each stacking, the PBE gap involved the same transition and was of similar magnitude (∼0.1 eV) to the PW91 gap, so only the latter data were tabulated. Band gaps were predominantly indirect for every functional. Every gap (e.g. K → M) calculated here has been cited in previous publications so we are confident in our results.

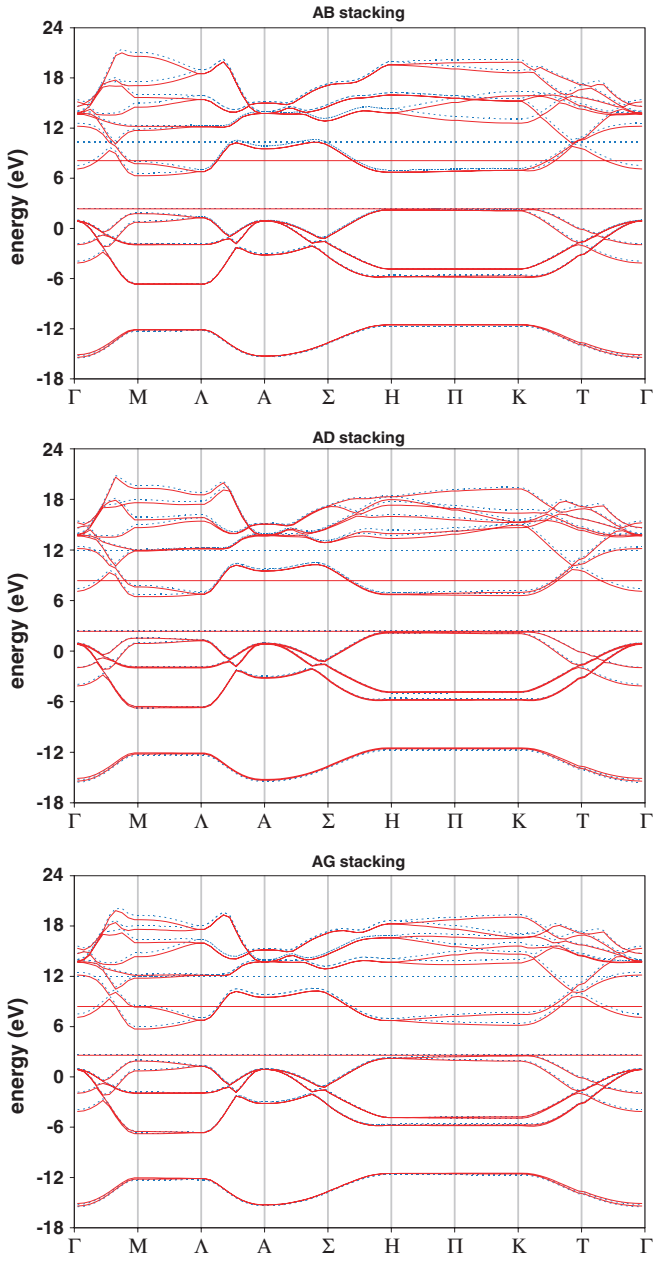


**Figure 8.** Band diagrams of several different stackings.

There are two principal differences between the band diagram for the isolated plane, and those for the four-atom cells. First, for a given functional, the band gaps calculated for the different stackings were about 0.3–1.2 eV less than those obtained for the isolated plane. Second, for the isolated plane, the bands along the Σ–T path of the BZ are symmetric about the middle of this region, the $\pi$ point. Likewise, bands along the M–Λ path are also symmetric about the middle of this path. This symmetry about the middle of the regions is lost in the

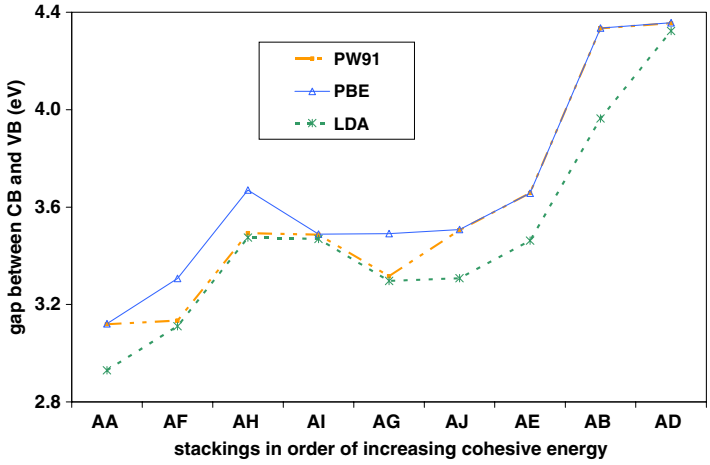


**Figure 9.** Band gap energy versus stacking.

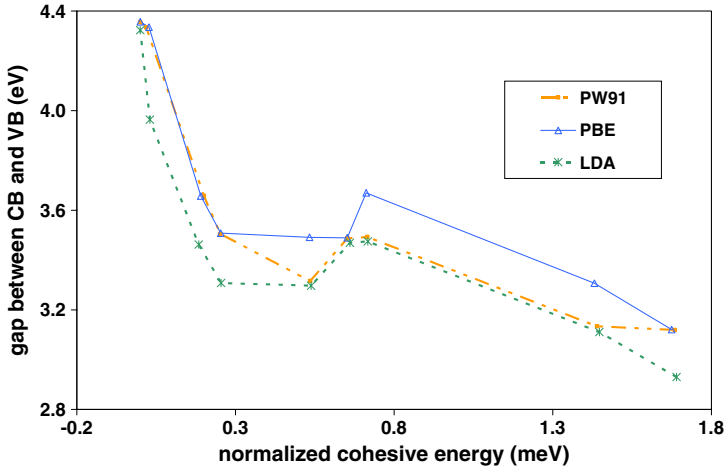


**Figure 10.** Band gap energy versus cohesive energy.

band diagrams for the four-atom unit cells. Both differences are due to interactions between adjacent planes.

One issue largely unexplored in the h-BN experimental literature is how the stacking affects the band structure. We examine this topic by seeing how the band gap is related to the stacking. From table 4, the ordering of stackings by the $E_C$ magnitude is identical for all three functionals, showing that the relative stabilities of different stackings are identical from either the LDA or GGA. The band gap is then plotted as a function of stacking to see if there is a consistent trend across all three functionals; see figure 9. On the $x$-axis, the stackings are arranged from left to right in order of increasing $E_C$. The band gap for each stacking is then plotted along the $y$-axis. The plots show similar trends for all three functionals such that AA has the smallest band gap and AD and AB have the largest gaps. The overall trend is a direct relationship between band gap size and $E_C$.

Taking the $E_C$ as a measure of bond strength; this $E_C$–band gap relationship is also seen in the zinc-blende semiconductors. For example, both band gap and bond strength decrease

going from diamond to Si to Ge. This behaviour can be understood in terms of a molecular orbital approach. The stronger the bond between two atoms, the lower in energy the bonding orbital drops and the higher in energy the anti-bonding orbital becomes, thereby increasing the energy gap between them. The question remains as to why the different stackings have different $E_C$ values. This is due to interplanar bonding, and is most easily explained for the extreme cases. In AA, ions in one plane sit atop ions of the same type in the adjacent plane, thereby maximizing ionic repulsion between planes and giving the smallest $E_C$ of all the stackings. In AB and AD, ions in one plane sit atop ions of the opposite type in adjacent planes, thereby maximizing ionic attraction between planes and producing the largest $E_C$ values. Note that the difference in $E_C$ between AA and AD is $<2$ meV/atom.

AG, AI, and AH deviate slightly from this direct $E_C$–band gap relationship. The reasons for this are unclear, though since they are the only stackings where atoms of one plane sit above the $sp^2$ bonds in the adjacent planes, there could be some interactions between the core electrons on one atom and the bonding electrons in the adjacent plane. To further clarify the $E_C$–band gap relationship, the band gap is plotted as a function of $E_C$. $E_C$ values differ by $\sim$1 eV across the three functionals but the range of values for a given functional vary by under 0.03 eV. Therefore, the $E_C$ of each stacking is defined with respect to the $E_C$ of AD, where the latter is set to zero. The band gaps are then plotted against this 'normalized' $E_C$ in figure 10. Like in the previous graph, the six points corresponding to AA, AB, AD, AE, AF, and AJ show a direct relationship between $E_C$ and band gap. Stackings AG, AH, and AI deviate from this trend.

## 7. Summary

Several conclusions can be drawn from our calculated results. First, the various ways in which adjacent planes can be stacked on top of each other in h-BN lead to structures of different symmetries, but similar cohesive energies, suggesting that basal plane sliding is easy. The relative stabilities of the different stackings were identical as calculated using each functional. Second, in-plane bondings as described by the band diagram, DOS, and ELF are very similar using the LDA and GGA. The differences in electronic structure between different XC functionals are then due to interactions between basal planes, which in turn are affected by the stacking. Third, h-BN has 2.9–4.5 eV band gap depending on the stacking, with the LDA band gap being slightly ($<1$ eV) higher than the GGA band gap. These calculated band gap values are at the low end of the 3–7.5 eV experimental range, and do not explain the large range of experimental values. Fourth, the band gap is indirect for the isolated basal plane and in most of the stackings examined, with the VB maximum in the H–T region of the BZ, with it usually near the K point in most of the stackings. The band gap is slightly larger for the isolated plane than for the four-atom unit cells, though the general features are similar for the two. Last, there is an approximately direct relationship between the gap size and the $E_C$ across the different stackings. These studies of the electronic structure of the h-BN plane and unit cells of different stackings have no parallel in experimental literature, which limits our ability to validate our data.

## Acknowledgments

We would like to acknowledge the National Center for Supercomputing Applications (NCSA) at the University of Illinois at Urbana Champaign (UIUC) for providing computational resources through grant number DMR000015N. We thank the members of the Computational Materials Science group at Arizona State University for help in performing calculations. We thank L G Hector Jr and Yue Qi at General Motors Research Laboratories, and the authors of VASP for help with using and understanding the VASP software. Last, we acknowledge Mark van Schilfgaarde for insightful discussion on the use of simulations in studying boron nitride.

## References


[1] Edgar J H 1994 *Properties of Group III Nitrides* (London: INSPEC)
[2] Muramatsu Y, Kaneyoshi T, Gullikson E M and Perera R C C 2003 *Spectrochim. Acta* A **59** 1951–7
[3] Yamamura S, Takata M and Sakata M 1997 *J. Phys. Chem. Solids* **58** 177–83
[4] *Handbook of Chemistry and Physics* 2005 (Boca Raton, FL: CRC Press)
[5] Lipp A, Schwetz K A and Hunold K 1989 *J. Eur. Ceram. Soc.* **5** 3–9
[6] Zhang Y, He X, Han J and Du S 2001 *J. Mater. Process. Technol.* **116** 161–4
[7] Choi B J 1999 *Mater. Res. Bull.* **34** 2215–20
[8] Watanabe S, Miyake S and Murakawa M 1991 *Surf. Coat. Technol.* **49** 406–10
[9] Kimura Y, Wakabayashi T, Okada K, Wada T and Nishikawa H 1999 *Wear* **232** 199–206
[10] Lelonis D A *et al* 2003 *General Electric Company Publication* No 81506
[11] Lelonis D A 2003 *General Electric Company Publication* No 81505
[12] Meunier V, Roland C, Bernholc J and Nardelli M B 2002 *Appl. Phys. Lett.* **81** 46–8
[13] Abdellaoui A, Bath A, Bouchikhi B and Baehr O 1997 *Mater. Sci. Eng.* B **47** 257–62
[14] Solozhenko V L, Lazarenko A G, Petitet J P and Kanaev A V 2001 *J. Phys. Chem. Solids* **62** 1331–4
[15] Watanabe K, Taniguchi T and Kanda H 2004 *Nat. Mater.* **3** 404–9
[16] Loh K P, Sakaguchi I, Gamo M N, Tagawa S, Sugino T and Ando T 1999 *Appl. Phys. Lett.* **74** 28–30
[17] Hohenberg P and Kohn W 1964 *Phys. Rev.* B **136** 864–71
[18] Furthmuller J, Hafner J and Kresse G 1994 *Phys. Rev.* B **50** 15606–22
[19] Kern G, Kresse G and Hafner J 1999 *Phys. Rev.* B **59** 8551–9
[20] Kim E and Chen C 2003 *Phys. Lett.* A **319** 384–9
[21] Cappellini G, Satta G, Palummo M and Onida G 2001 *Phys. Rev.* B **64** 035104–14
[22] Mosuang T E and Lowther J E 2002 *Phys. Rev.* B **66** 014112–6
[23] Mosuang T E and Lowther J E 2000 *J. Phys. Chem. Solids* **63** 363–8
[24] Janotti A, Wei S H and Singh D J 2001 *Phys. Rev.* B **64** 174107–11
[25] Yu W J, Lau W M, Chan S P, Liu Z F and Zheng Q Q 2003 *Phys. Rev.* B **67** 014108–16
[26] Solozhenko V L 1994 *Diamond Relat. Mater.* **4** 1–4
[27] Liu L, Feng Y P and Shen Z X 2003 *Phys. Rev.* B **68** 104102–9
[28] Xu Y N and Ching W Y 1991 *Phys. Rev.* B **44** 7787–98
[29] Kresse G and Furthmuller J 1996 *Phys. Rev.* B **54** 11169–86
[30] Blochl P E 1994 *Phys. Rev.* B **50** 17953–79
[31] Kresse G and Joubert D 1999 *Phys. Rev.* B **59** 1758–75
[32] Rappe A M, Rabe K M, Kaxiras E and Joannopoulos J D 1990 *Phys. Rev.* B **41** 1227–30
[33] Ceperley D M and Alder B J 1980 *Phys. Rev. Lett.* **45** 566–9
[34] Perdew J P *et al* 1992 *Phys. Rev.* B **46** 6671–87
[35] Perdew J P, Burke K and Ernzerhof M 1996 *Phys. Rev. Lett.* **77** 3865–8
[36] Pulay P 1980 *Chem. Phys. Lett.* **73** 393–8
[37] Broyden C G 1965 *Math. Comput.* **19** 577–93
[38] Johnson D D 1988 *Phys. Rev.* B **38** 12807–13
[39] Blochl P E, Jepsen O and Andersen O K 1994 *Phys. Rev.* B **49** 16223–33
[40] Methfessel M and Paxton A T 1989 *Phys. Rev.* B **40** 3616–21
[41] Becke A D and Edgecombe K E 1990 *J. Chem. Phys.* **92** 5397–403
[42] Savin A and Silvi B 1994 *Nature* **371** 683–6
[43] Savin A, Nesper R, Wengert S and Fassler T F 1997 *Angew. Chem. Int. Edn Engl.* **36** 1808–32